# CHARACTERISATION OF BAUXITE RESIDUE AND SEAWATER NEUTRALISED BAUXITE RESIDUE USING VIBRATIONAL SPECTROSCOPIC TECHNIQUES

Palmer SJ*, Frost RL and Reddy BJ

*Inorganic Materials Research Program, School of Physical and Chemical Sciences, Queensland University of Technology, QLD, Australia*

## Abstract

Bauxite refinery residues are derived from the Bayer process by the digestion of crushed bauxite in concentrated caustic at elevated temperatures. Chemically, it comprises, in varying amounts (depending upon the composition of the starting bauxite), oxides of iron and titanium, residual alumina, sodalite, silica, and minor quantities of other metal oxides. Bauxite residues are being neutralised by seawater in recent years to reduce the alkalinity in bauxite residue, through the precipitation of hydrotalcite-like compounds and some other Mg, Ca, and Al hydroxide and carbonate minerals.

A combination of X-ray diffraction (XRD) and vibrational spectroscopy techniques, including mid-infrared (IR), Raman, near-infrared (NIR), and UV-Visible, have been used to characterise bauxite residue and seawater neutralised bauxite residue. Both the ferrous ($Fe^{2+}$) and ferric ($Fe^{3+}$) ions within bauxite residue can be identified by their characteristic NIR bands, where ferrous ions produce a strong absorption band at around 9000 $cm^{-1}$, while ferric ions produce two strong bands at 25000 and 14300 $cm^{-1}$. The presence of adsorbed carbonate and hydroxide anions can be identified at around 5200 and 7000 $cm^{-1}$, respectively, attributed to the 2nd overtone of the 1st fundamental overtones observed in the mid-IR spectra. The complex bands in the Raman and mid-IR spectra around 3500 $cm^{-1}$ are assigned to the OH stretching vibrations of the various oxides present in bauxite residue, and water. The combination of carbonate and hydroxyl units and their fundamental overtones give rise to many of the features of the NIR spectra.

---

## 1. Introduction

Bauxite refinery residues (red mud) are derived from the Bayer process by the digestion of crushed bauxite in concentrated caustic (NaOH) at elevated temperatures [1]. Digestion temperatures are dependent on the quantity of gibbsite (γ-Al(OH)$_3$), boehmite (γ-Al(O)OH), and diaspore (α-Al(O)OH) present in the bauxite ore. Bauxites containing predominantly gibbsite require lower digestion temperatures (145 - 175 ℃), while those with high boehmite and diaspore require stronger caustic concentrations and temperatures (245 - 275 ℃) [2]. The process results in the dissolution of gibbsite (Al(OH)$_3$) and boehmite as sodium aluminate, while the remaining insoluble residue (45% liquor and 55% solid mud), known widely as red mud (RM), is removed by means of flocculation and decantation [1, 3]. The exact composition of the fine textured residue depends on the initial type of bauxite. Roughly 1.0 to 1.5 tonnes of red mud residue is produced for every tonne of alumina produced, therefore millions of tonnes of red mud is produced annually. The liquor is strongly alkaline (pH ranging from 10 to 13) [4] and requires neutralisation to a pH below 9, with an optimum pH value of 8.5 to 8.9 [5], before becoming environmentally benign.

Red mud (RM) varies in physical, chemical, and mineralogical properties due to differing bauxite ore sources and refining processes employed [6, 7]. The general consensus of the composition of red mud has been found to be largely composed of iron oxides, primarily hematite (Fe$_2$O$_3$), and goethite ((FeOOH), boehmite (AlOOH), other aluminium hydroxides, calcium oxides, titanium oxides (anatase and rutile), and aluminosilicate minerals (sodalite) [3, 6-8]. Charged lime species may also be present. These minerals are the chemically stable end products of bauxite formation and refining, and are the components responsible for the high surface reactivity of red mud [1, 3, 6, 8].

Bauxite refinery residues are characterised by relatively high concentrations of sodium aluminate and sodium carbonate and a variety of anionic species. If left untreated, these species have the potential to be detrimental to the environment. Therefore, systems have been developed to remove these species prior to disposal. A number of alumina refineries have implemented the neutralisation of red mud with seawater, and found it provided a reduction in both pH and dissolved metal concentrations [5, 8]. Glenister and Thornber, [5], concluded disposal of refinery residues at pH 8 was optimal, since at this pH chemically adsorbed Na is released, neutralising alkaline buffer minerals and rendering most of the dissolved metal species insoluble. Seawater neutralisation results in the neutralisation of alkalinity through the precipitation of Mg, Ca, and Al hydroxide and carbonate minerals, where the formation of hydrotalcite-like compounds become favoured as the pH begins to reach its neutralisation point. The carbonate and bicarbonate alkalinity of the waste is primarily removed through the precipitation of calcite and aragonite [9].

Minerals containing oxidised iron (Fe$^{3+}$), such as hematite in red mud, have a characteristic red colour. The spectra of Fe$^{3+}$ minerals exhibit electronic transitions localised to the FeO$_6$ coordination site. Sherman and Waite [10], synthesised several Fe$_2$O$_3$ and FeOOH polymorphs (hematite, maghemite, goethite, lepidocrocite) and analysed their spectra in the near IR to UV. The report showed that these minerals consisted primarily of Fe$^{3+}$ ligand filed transitions [10]. Characterisation of red mud is made possible by the effect of structural cationic substitutions (Al$^{3+}$, Fe$^{3+}$, Ti$^{3+}$, Ca$^{2+}$, Fe$^{2+}$) on band shifts in the high wavenumber region, 40,000-7500 $cm^{-1}$ and vibrational modes of carbonate ion and OH units in the region 7300 to 4000 $cm^{-1}$.

The objective of this investigation is to characterise red mud, before and after seawater neutralisation. Determination of any changes in the composition of red mud was then identified to help determine the possible reactions that take place during the seawater neutralisation process. Due to the complexity of red mud the identification of the components present in red mud is difficult. The result of the work will be used for further investigations on the mechanism/s involved in the seawater neutralisation process. The UV-Vis-NIR diffuse reflectance spectroscopy (DRS) approach was undertaken to study the cationic distribution in red mud before and after seawater neutralisation.

## 2. Experimental

The Queensland Research and Development Centre (QRDC) Rio Tinto Alcan provided red mud from a Rio Tinto Alumina refinery. Seawater neutralised (SWN) red mud was prepared by treating red mud with 4.5 times the volume of seawater in a dropwise fashion. Characterisation of red mud and SWN red mud included: X-ray diffraction, Raman spectroscopy, IR spectroscopy, UV-Vis spectroscopy, and Near-IR spectroscopy. X-Ray diffraction patterns were collected using a Philips X'pert wide angle X-Ray diffractometer, operating in step scan mode, with Co Kα radiation (1.78897Å). Raman spectra were excited by a HeNe laser (633 nm) at a nominal resolution of 2 cm$^{-1}$ in the range between 100 and 4000 cm$^{-1}$, using a Renishaw 1000 Raman BHSM microscope.

Infrared spectra (over the 4000-525 cm$^{-1}$ range) were obtained using a Nicolet Nexus 870 FTIR spectrometer with a smart endurance single bounce diamond ATR cell. A Varian Cary 5000 UV-Visible NIR spectrophotometer, equipped with Diffuse Reflectance Accessory (DRA) was employed to record the electronic spectrum of the samples in the region between 200 and 1100 nm (50,000-9090 cm$^{-1}$). NIR spectra were collected on a Nicolet Nexus FT-IR spectrometer with a Nicolet Near-IR Fibreport accessory (Madison, Wisconsin). Spectra were obtained from 13,000 to 4000 cm$^{-1}$ (0.77-2.50 μm) by the co-addition of 128 scans at a spectral resolution of 8 cm$^{-1}$.

## 3. Results and discussion

### 3.1 X-ray diffraction

Due to the complexity of red mud numerous mineralogical phases were identified using XRD. The XRD patterns of red mud and SWN red mud are given in Figure 1, with major peaks labelled. The XRD pattern obtained for red mud (RM) and SWN-RM show that hematite and gibbsite are the major components present. XRD results identified 12 different mineralogical phases present in RM and SWN-RM, table not given, with the exception that SWN-RM showed an additional mineralogical phase, hydrotalcite. These results are in good agreement with literature [11]. The seawater neutralisation process produces hydrotalcite-like compounds through the neutralisation of free OH$^-$ with Mg, Al, and Ca to form hydroxycarbonates. Other compounds such as boehmite, cancrinite, whewellite, anatase, calcite, and quartz were some of the other phases detected. Variations in reported values and components of seawater neutralised red mud are due to the differences in physical, chemical, and mineralogical properties of red mud.

Changes in XRD patterns of hematite and gibbsite are shown in Figure 1. The comparison of the XRD patterns of RM and SWN-RM shows that there is a slight reduction in the intensity of the hematite peaks, and a more significant decrease in intensity was observed for gibbsite at 18 2θ°. A decrease in the intensity of this peak indicates a phase transition of gibbsite occurs. The small changes in intensity suggest hematite and gibbsite are involved in chemical reactions during the seawater neutralisation process. These observations agree with those of Sherman and Waite [10]. A broad peak at approximately 12 2θ° is characteristic of the d$_{(003)}$ peak for hydrotalcite (Mg$_6$Al$_2$(OH)$_{16}$(CO$_3$).4H$_2$O), [11], which is produced during the seawater neutralisation process. The weak intensity of this peak is due to the overshadowing of the sharper and more crystalline mineralogical phases. The broadness of the hydrotalcite peak suggests poor crystallinity, due to a short formation period. Synthetic hydrotalcites were prepared in the absence of RM and found that the same broadness was observed. Other components such as sodium aluminium silicate hydrate (SASH) and boehmite appear to be unaffected by the seawater neutralisation process.

### 3.1 Raman Spectroscopy

The Raman spectra for RM and SWN-RM are shown in Figure 2. The broadness of the bands indicates multiple components are present in the same wavenumber region, and therefore band component analysis was carried out. The rich red colour of red mud is due to iron oxides, in particular hematite. Hematite belongs to the D3$_{6d}$ crystal space group and seven phonon lines are expected in the Raman spectrum, namely two A$_{1g}$ modes (225 and 498 cm$^{-1}$) and five E$_g$ modes (247, 293, 299, 412 and 613 cm$^{-1}$) [12]. Peaks assigned to hematite dominate the spectra due to the large quantity of hematite in the samples. Peaks at 223, 246$^*$, 291, 408, 610, 658 and 1318 cm$^{-1}$ were observed for RM and are in good agreement with the values reported [12]. Similar peaks have been observed in SWN-RM at 225, 247$^*$, 292, 408, 613, 660 and 1324 cm$^{-1}$. Band positions with $^*$ were determined by band component analysis, figures not shown. The peak at 1320 cm$^{-1}$ has been previously reported by Hart *et al.*, [13], and was assigned to the 2-magnon scattering of hematite. The very intense peak at around 145 cm$^{-1}$ is ascribed to the O-Ti-O bending vibration associated with anatase. The band at 145 cm$^{-1}$ could belong to either anatase or rutile (both of which are present in red mud), however it was ascribed to anatase as the intensity of the peak is strong, unlike the rutile peak. Five bands are assigned to anatase, the two strongest bands are located at 146 and 638$^*$ cm$^{-1}$, and three weaker bands at around 199$^*$, 397$^*$, and 514$^*$ cm$^{-1}$ [14]. All bands reported by Murad, [14], were observed in this investigation. Bands at around 1400, 509, 223, and 197 cm$^{-1}$ are attributed to whewellite (Ca(C$_2$O$_4$).H$_2$O) [15], an organic impurity found in red mud. Other components detected using Raman spectroscopy were gibbsite, boehmite, calcite, and quartz, Table 1.

Cancrinite and sodalite are common sodium aluminosilicate compounds that form in strongly caustic alkaline aqueous solutions. Cancrinite has characteristic Raman band positions at 1057, 524, 469, and 443 cm$^{-1}$, where the band at around 1057 cm$^{-1}$ is attributed to the anti-symmetric stretch, v(Al-O-Si) of the aluminosilicate framework [16]. Bands at lower wavenumbers are attributed to the symmetric stretch of the aluminosilicate framework [16]. The Raman spectra of both red mud and SWN red mud show these characteristic band positions, however slight shifts to lower wavenumbers was observed. The band at around 440 cm$^{-1}$ is of particular interest, as an increase in the intensity of this band was observed for the SWN red mud. This suggests that the quantity of cancrinite in red mud increases when seawater neutralised, possibly due to the transformation of sodalite to cancrinite. Studies have shown that sodalite transforms to cancrinite (Na$_6$Ca$_{1.5}$Al$_6$Si$_6$O$_{24}$(CO$_3$)$_{1.6}$) over time [17]. However, variations exist in literature in regards to the rate of transformation.

### 3.3 Infrared Spectroscopy

#### 3.3.1 Hydroxyl Stretching Region

Water hydroxyl-stretching vibrations are intense in infrared spectroscopy because of the large change in dipole moment. However, water is a very weak Raman scatterer and the v(OH) modes are not as intense in a Raman spectrum. Due to fluorescence in the Raman spectra no bands were detected in the water hydroxyl-stretching vibrational region. The infrared spectra of the hydroxyl stretching region of red mud and SWN red mud are given in Figure 3. Both the red mud and SWN red mud show a broad, intense band centred at approximately 3400 cm$^{-1}$, due to the stretching modes of hydroxyl groups and water molecules in the aluminium, iron, silica, titanium and calcium oxides. The broadness of this absorption indicates that these species are hydrogen bonded [18]. Both RM and SWN-RM show a complicated spectrum with up to 16 infrared hydroxyl-stretching bands being observed. The assignment of the bands is difficult

because of the initial complex band profile and the overlap of bands.

Infrared absorption bands located at around 3618, 3520, 3428, and 3380 cm$^{-1}$ are assigned to the $v$(OH) stretching modes of gibbsite [19, 20]. For red mud four infrared absorption bands were observed at 3618, 3522, 3420, and 3374 cm$^{-1}$, and two infrared emission bands were observed at 3355 and 3476 cm$^{-1}$. For SWN red mud four infrared absorption bands were observed at 3618, 3523, 3424, and 3373 cm$^{-1}$, and two infrared emission bands were observed at 3356 and 3488 cm$^{-1}$. The band positions observed are in good agreement with those reported by Frost, [20], and Farmer, [19]. The intensity of bands at 3618 and 3522 cm$^{-1}$ decrease after seawater neutralisation, which agrees with the results found by XRD analysis that a phase transition occurs. The bands assigned to gibbsite appear as the sharper bands in the infrared spectra. The hydroxyl deformation modes of gibbsite were observed at 1069, 1030, 964, and 913 cm$^{-1}$ for RM, and for SWN red mud the bands are observed at 1066, 1031, 972, and 915 cm$^{-1}$. These observations are in good agreement with those reported [20]. Broader peaks at lower wavenumbers are assigned to boehmite [19, 21]. For red mud the infrared absorption bands for boehmite were observed at 3299, 3094, and 3009 cm$^{-1}$, and for SWN red mud, the infrared absorption bands were located at 3304, 3096, and 3005 cm$^{-1}$. Bands associated with whewellite were also observed.

The surfaces of hematite crystals are covered with hydroxyl groups, and although they are not structural OH groups, the vibrations of which can appear in the infrared spectrum. Rochester and Topham, [22] reported eleven such bands the most significant of which were at 3720 (shoulder), 3700, 3635, 3490 (shoulder), 3435 (shoulder), and 3380 cm$^{-1}$. Even though hematite was detected using XRD and Raman spectroscopy, none of these bands were observed in the IR spectra. It is suggested that surface hydroxyl groups were removed during the drying process, therefore expected bands were weak and undetectable.

### 3.3.2 Carbonate vibrations

The infrared spectra of red mud and SWN red mud in the region 1800-1200 cm$^{-1}$ is highly complex with multiple bands that overlap, shown in Figure 4. Interpretation of the individual bands is difficult, due to the number of carbonates present in red mud. Carbonates generally show strong infrared absorptions in the region 1450-1400 cm$^{-1}$ ($v_3$), medium absorption bands between 890 and 800 cm$^{-1}$ ($v_2$), and at 760-670 cm$^{-1}$ ($v_4$) [23]. Carbonates that are of aragonite-type observe the symmetric stretch ($v_1$) at around 1120-1040 cm$^{-1}$ [23]. Figure 4 shows a broad band stretching from 1700 to 1300 cm$^{-1}$ with multiple bands in the $v_3$ region, suggesting that there are several carbonates present in both red mud and SWN red mud. Four infrared absorption bands are observed at 1475, 1440, 1452 and 1401 cm$^{-1}$ for red mud, and at 1475, 1441, 1451, and 1409 cm$^{-1}$ for SWN red mud. No significant changes in the $v_3$ band positions were observed. The $v_4$ and $v_2$ vibrational modes were observed, however figures are not shown.

Typically red mud contains 2-8wt% calcite (CaCO$_3$). Five vibrational frequencies are expected for calcite; 1444, 1435, 1099, 876, 724, and 712 cm$^{-1}$ [19]. The infrared spectra of red mud and SWN red mud show similar bands as reported by Farmer [19]. Five of the six infrared bands for calcite were observed at 1440, 1433, 1096, 875, and 724 cm$^{-1}$ for red mud. The corresponding bands for calcite for SWN red mud were observed at 1441, 1432, 875, and 728 cm$^{-1}$. The intensity of the calcite peak at 1440 and 1433 cm$^{-1}$ decreased after neutralisation slightly. It's suggested that a slight dissolution of calcite occurred.

Sodalite has characteristic infrared bands at 1000 cm$^{-1}$ attributed to the anti-symmetric stretch of the Al-O-Si framework, with symmetric frequencies located at 737, 713, and 668 cm$^{-1}$ [16]. Cancrinite (Na$_6$Ca$_{1.5}$Al$_6$Si$_6$O$_{24}$(CO$_3$)$_{1.6}$) also exhibits carbonate vibrations at 1505, 1480, 1438, 1400-1390 cm$^{-1}$ [19]. Four infrared bands were observed for red mud at 1503, 1480, 1440, and 1401 cm$^{-1}$, and at 1492, 1475, 1441, and 1409 cm$^{-1}$ for SWN red mud. Bands at 1363, and 1334 cm$^{-1}$, 1372, and 1352 cm$^{-1}$, for red mud and SWN red mud respectively, are characteristic infrared bands of whewellite (Ca(C$_2$O$_4$).H$_2$O). It appears the quantity of whewellite increases after neutralisation, the intensity of 1363 and 1334 cm$^{-1}$ in SWN red mud increased significantly. The increase in whewellite is believed to be due to the increase in free Ca$^{2+}$ ions introduced through the addition of seawater that then complexes with oxalic acid in solution, forming whewellite.

### 3.4 UV-Vis spectroscopy

The spectra of Fe$^{3+}$ (O/OH)$_6$ group of minerals in the extended UV-Vis region to NIR include two broad bands near 650nm and 900 nm and one sharp band at 400 nm [10, 24, 25]. The optical absorption spectra in the UV-VIS-NIR (VNIR) of red mud and SWN red mud (SWN-RM) are shown in Figure 5. The bands are diffuse and weak in intensity due to the Fe$^{3+}$ transitions being spin-forbidden [26]. The individual bands were resolved by the application of component analysis. The broad band centred around 860 nm (11630 cm$^{-1}$) with a shoulder near 665 nm (15030 cm$^{-1}$) in Figure 5 are assigned to 6A1g(S) → 4T1g(G) and 6A1g(S)→4T2g(G) transitions [27, 28]. Band component analysis identified the splitting of the band at around 18700 cm$^{-1}$ into two components, 552 and 520 nm (18115 and 19240 cm$^{-1}$). These bands are a characteristic feature of ferric ion and are attributed to the 6A1g(S) → 4Eg,4A1g(G) transition. The two weak bands on the UV side of the spectrum at 400 and 313 nm (25000 and 31985 cm$^{-1}$) are determined from the Tanabe-Sugano diagram for the Fe$^{3+}$ ion, and are ascribed to the 6A1g(S) → 4T2g(D) and 6A1g(S)→4T1g(P) transitions [29]. The observed band energies and their assignments are given in Table 2 and are compared with assignments of Fe$^{3+}$ bands in Fe$_2$O$_3$ and FeOOH polymorphs reported by Sherman and Waite [10]. The data relates closely with hematite. However, the deviation in values may be due to the complexity of red mud, where it is a mixture of both oxides and oxide hydroxides of iron. The VNIR spectra clearly show that peak maxima are observed at slightly different positions for the red mud and SWN red mud, however the spectral patterns are very similar. The similarity of the spectra of red mud before and after seawater neutralisation suggests that there is no influence of seawater neutralisation on structural ferric ion.

### 3.5 Near-infrared spectroscopy

NIR spectroscopy displays electronic spectral features of transition metal ions at higher energies (13000-7500 cm$^{-1}$), and vibration bands of anions and molecules from 7300-4000 cm$^{-1}$. A broad band centred at 11630 cm$^{-1}$ (860 nm) in the UV-VIS spectrum appeared as a strong broad band at ~11300 cm$^{-1}$ in the near-infrared spectrum, figure not shown, with a splitting of two component bands at 11770 and 10940 cm$^{-1}$. These bands are characteristic of the 6A1g(S) → 4T1g(G) transition band [10, 24] of Fe$^{3+}$ with octahedral coordination. Spectra of H$_2$O-bearing minerals like biotite, pyrophyllite, epidote, and illite give rise to overtones of OH at ~1.4 μm (7145 cm$^{-1}$) and for water near 1.9 μm (5265 cm$^{-1}$) [30]. The NIR spectral profile in the 7300-6700 cm$^{-1}$ region, Figure 6, represents bands due to overtones of OH-stretching fundamental modes. The band centred at 7050 cm$^{-1}$ with a shoulder band at 7150 cm$^{-1}$ is attributed to FeOH and AlFeOH groups of oxyhydroxides of iron and aluminium related minerals in red mud. The structural band located at 6895 cm$^{-1}$ observed with components on either side at 6955 and 6845 cm$^{-1}$ are assigned to the overtones of OH-stretching fundamental modes of (SiSi)O-OH.

The combination bands of the hydroxyl stretching and deformation vibrations observed in the 5400 to 4200 cm$^{-1}$ region are shown in Figure 7. One weak band observed at 5210 cm$^{-1}$ indicates molecular $H_2O$ adsorbed on red mud. The combination of metal-OH bending and OH stretching has been observed in minerals near 2.20-2.30 μm (4545-4350 cm$^{-1}$) [30]. The strongest band observed in the spectrum was at 4405 cm$^{-1}$ with shoulders at 4440 and 4375 cm$^{-1}$, attributed to combination and overtone modes of carbonate ($CO_3^{2-}$) fundamentals. The observation of the overtones of carbonate ion is in harmony with natural and synthetic aurichalcites that include a series of five bands around 5200, 5000, 4800, 4400 and 4200 cm$^{-1}$ [31]. The band near 4600 cm$^{-1}$ is assigned to Al-OH, and appears weak due to overlapping of carbonate bands in the same region. A low intensity peak at 4310 cm$^{-1}$ is due to Fe-OH vibrations.

## Conclusions

The characterisation of red mud and seawater neutralised red mud proved difficult due to the complex band profile with multiple overlapping bands. However, major constituents of red mud could be identified. XRD identified 12 different mineralogical phases present in red mud and 13 mineralogical phases in SWN red mud. The additional phase in SWN red mud is due to the formation of hydrotalcite during the seawater neutralisation process. The majority of the peaks identified in the Raman spectra were ascribed to hematite, which makes up to 60 wt%

of bauxite refinery residues. However, in the infrared spectra hematite was not clearly identified. The complex band profile of the hydroxyl-stretching vibrational region of the infrared spectra was determined to be attributed to gibbsite and boehmite, which are also major mineralogical phases present in red mud. Both XRD and IR techniques observed a decrease in the quantity of gibbsite after seawater neutralisation and it is believed a phase transition is responsible for this observation. A similar observation was also seen for hematite. Due to the abundance of carbonate compounds in red mud, multiple bands were observed in the carbonate vibrational region. Bands assigned to whewellite increased in intensity after seawater neutralisation due to the complexation of $Ca^{2+}$ in seawater with oxalic acid in the red mud slurry. IR and Raman identified different mineralogical phases of red mud, therefore a combination of these techniques is required to study the bauxite refinery residues.

The observation of two broad bands in red mud and SWN-RM near 860 and 400 nm (11300 and 25000 cm$^{-1}$) and a pair of sharp bands centred at 500 nm (20000 cm$^{-1}$) are characteristic features of the $Fe^{3+}$. The observation of identical spectral patterns (both electronic and vibrational spectra) of red mud before and after seawater neutralisation confirmed that there is no effect of seawater neutralisation on structural cationic substitutions such as $Al^{3+}$, $Fe^{3+}$, $Fe^{2+}$, $Ti^{3+}$.

## Tables

Table 1. Raman wavenumbers and relative intensities (vs = very strong, s = strong, m = medium, and w = weak) for RM and SWN-RM [15, 19, 20, 23].

| Red mud samples | | Reference Wavenumbers | | | | | | | |
|---|---|---|---|---|---|---|---|---|---|
| Red mud | SWN-RM | Hematite | Cancrinite | Whewellite | Gibbsite | Boehmite | Calcite | Anatase | Quartz |
| **1398 (m)** | **1400 (m)** | | | 1402 | | | | | |
| **1318 (s)** | **1324 (s)** | 1322 (s) | | | | | | | |
| 1084 (w) | 1111 (w) | | | | | | 1085 | | 1085 |
| 1048 (w) | 1069 (w) | | 1057 | | 1051 | 1072 | | | |
| 816 (w) | 823 (w) | | | 896 | 816 | | | | 811 |
| **658 (s)** | **660 (s)** | 657 (m) | | | | 674 | | | |
| **632 (m)** | **635 (s)** | | | | | | | 638 (m) | |
| **610 (s)** | **613 (s)** | 610 (m) | | 601 | 617 | | | | |
| **509 (w)** | **512 (w)** | | 524 | 509 | 506 | | | 514 (w) | 510 |
| 494 (w) | | 498 (w) | | | | 495 | | | |
| 457 (m) | | | 469 | | | 451 | | | 464 |
| **438 (s)** | **443 (s)** | | 443 | | 444 | | | | |
| **408 (s)** | **408 (s)** | 412 (s) | | | 412 | | | | |
| 398 (m) | 386 (m) | | | | 396 | 360 | | 397 (w) | |
| 303 (w) | 299 (w) | | 301 | | 306 | | | | |
| **291 (s)** | **292 (s)** | 293 (s) | 277 | | 290 | | 282 | | |
| 246 (w) | 247 (w) | 246 (w) | | 251 | 242 | | | | |
| **223 (s)** | **225 (s)** | 227 (s) | | 223 | | 228 | | | |
| **145 (vs)** | **143 (vs)** | | | 141 | | | | 146 (vs) | |

Table 2. Energies and assignments of the bands observed in red mud and a comparison with the assignments of $Fe^{3+}$ bands in the electronic spectra of iron oxides ($Fe_2O_3$) and oxide hydroxides (FeOOH).

| Transition | Observed band positions | | | | Reported band positions [10] | |
|---|---|---|---|---|---|---|
| | Red mud | | SWN red mud | | Hematite | Goethite |
| | λ(nm) | v(cm⁻¹) | λ(nm) | v(cm⁻¹) | v(cm⁻¹) | v(cm⁻¹) |
| $^6A_{1g}(S)\ ^4T_{1g}(G)$ | 860 | 11630 | 876 | 11420 | 11300 | 10900 |
| $^6A_{1g}(S)\ ^4T_{2g}(G)$ | 665 | 15030 | 664 | 15060 | 15400 | 15400 |
| $^6A_{1g}(S)\ ^4E_g,\ ^4A_{1g}(G)$ | 552 | 18115 | 554 | 18055 | 22500 | ~23000 |
| | 520 | 19240 | 522 | 19170 | | |
| $^6A_{1g}(S)\ ^4T_{2g}(D)$ | 400 | 25000 | 401 | 24910 | 24700 | nd |
| $^6A_{1g}(S)\ ^4E_g(D)$ | nd | nd | nd | nd | 26300 | 27400 |
| $^6A_{1g}(S)\ ^4T_{1g}(P)$ | 313 | 31985 | 310 | 32270 | 31300 | 35000 |

nd: not detected

## Figures
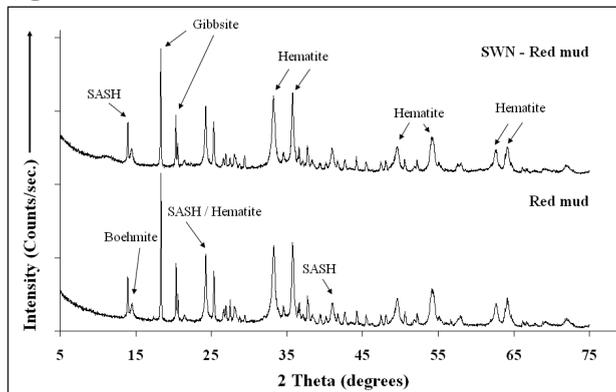


Figure 1. Comparison of the XRD patterns of RM and SWN-RM, where SASH represents Sodium Aluminium Silicate Hydrate
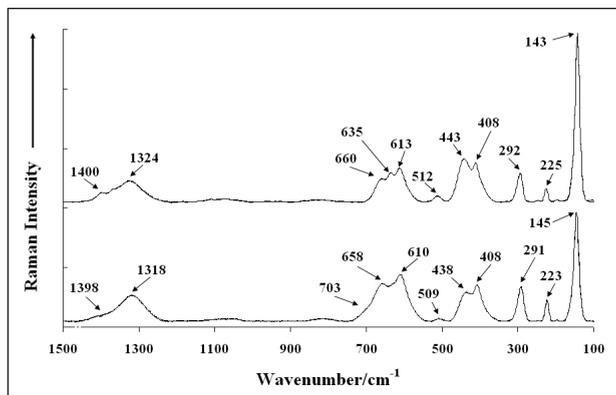


Figure 2. Raman spectra of red mud (bottom) and seawater neutralised red mud (top).



Figure 3. Infrared spectra of RM and SWN-RM in the 3800 – 2800 cm⁻¹
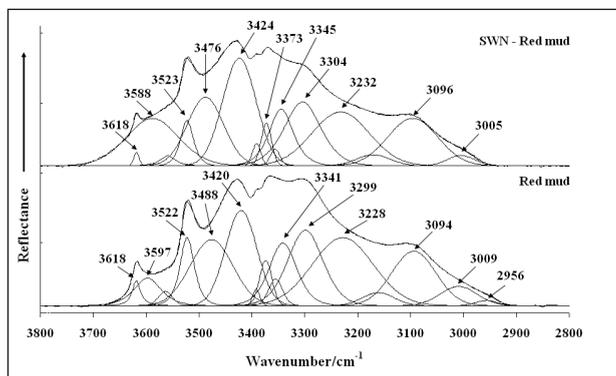


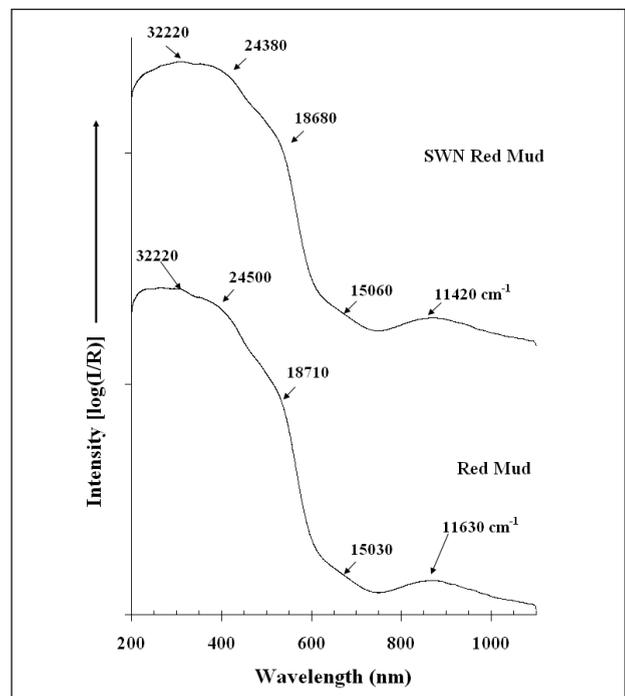Figure 4. Infrared spectra of RM and SWN-RM in the 1800 – 1200 cm⁻¹



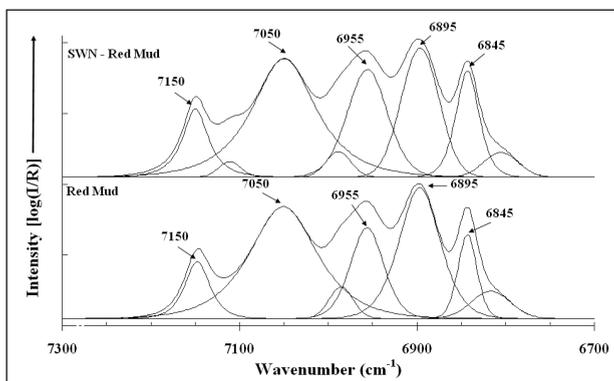Figure 5. Optical absorption spectra in the UV-VIS-NIR of RM and SWN-RM

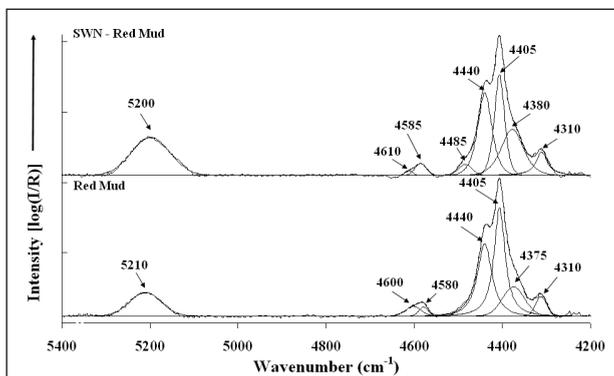Figure 6. NIR spectra of RM and SWN-RM of the fundamental overtones of OH-stretching modes



Figure 7. NIR spectra of RM and SWN-RM in the OH-stretching and deformation vibrational region

## References

1. Hind, A.R., Bhargava, S.K., Grocott, S.C., 1999, 'The surface chemistry of Bayer process solids: a review', Colloids and Surfaces A: Physicochemical and Engineering Aspects, vol. 146, no. 1-3, pp. 359-374.

2. Jamialahmadi, M., Muller-Steinhagen, H., 1998, 'Determining Silica Solubility in Bayer Process Liquor', JOM Journal of the Minerals Metals and Materials Society, vol. 50, no. 11, pp. 44-49.

3. Chvedov, D., Ostap, S., Le, T., 2001, 'Surface properties of red mud particles from potentiometric titration', Colloids and Surfaces A: Physicochemical and Engineering Aspects, vol. 182, no. 1-3, pp. 131-141.

4. Menzies, N.W., Fulton, I.M., Morrell, W.J., 2004, 'Seawater neutralization of alkaline bauxite residue and implications for revegetation', Journal of Environmental Quality, vol. 33, no. 5, pp. 1877-1884.

5. Glenister, D.J., Thornberg, M.R., 1985, 'Alkalinity of red mud and its application for the management of acid wastes', Chemica, vol. 85, pp. 100-113.

6. Diaz, B., Joiret, S., Keddam, M., Novoa, X.R., Perez, M.C., Takenouti, H., 2004, 'Passivity of iron in red mud's water solutions', Electrochemical Methods in Corrosion Research, vol. 49. no. 17-18, pp. 3039-3048.

7. Santona, L., Castaldi, P., Melis, P., 2006, 'Evaluation of the interaction mechanisms between red muds and heavy metals', Journal of Hazardous Materials, vol. 136, no. 2, pp. 324-329.

8. Hanahan, C., McConchie, D., Pohl, J., Creelman, R., Clark, M., Stocksiek, C., 2004, 'Chemistry of Seawater Neutralization of Bauxite Refinery Residues (Red Mud)', Environmental Engineering Science, vol. 21, no. 2, pp. 125-138.

9. McConchie, D., Clark, M., Hanahan, C., Davies-McConchie, F., 'The use of seawater-neutralised bauxite refinery residues in the management of acid sulphate soils, sulphidic mine tailings and acid mine drainage', 3rd Queensland Environmental Conference: Sustainable Solutions for Industry and Government, Brisbane, QLD, Australia, 2000, pp. 201-208.

10. Sherman, D.M., Waite, T.D., 1985, 'Electronic spectra of iron(III) oxides and oxide hydroxides in the near IR to near UV', American Mineralogist, vol. 70, no. 11-12, pp. 1262-1269.

11. Kloprogge, J.T., Wharton, D., Hickey, L., Frost, R.L., 2002, 'Infrared and Raman study of interlayer anions $CO_2$-3, $NO$-3, $SO_2$-4 and $ClO$-4 in Mg/Al-hydrotalcite', American Mineralogist, vol. 87, no. 5-6, pp. 623-629.

12. Porto, S.P.S., Krishnan, R.S., 1967, 'Raman effect of corundum', Journal of Chemical Physics, vol. 47, no. 3, p. 1009.

13. Hart, T.R., Adams, S.B., Tempkin, H., 1990, 'Effects of pressure and isotopic substitution on the Raman spectrum of $\alpha$-Fe2O3: Identification of two-magnon scattering', Physical Review, vol. 41, no. 11, pp. 7822-7827.

14. Murad, E., 1997, 'Identification of minor amounts of anatase in kaolins by Raman spectroscpoy', American Mineralogist, vol. 82, pp. 203-206.

15. Downs, R.T., 2006, 'The RRUFF project: an integrated study of the chemistry, crystallography, Raman and infrared spectroscopy of minerals, Retrieved: November 20, 2006, from http://rruff.info./

16. Hermeler, G., Buhl, J.C., Hoffmann, W., 1991, 'Influence of carbonate on the synthesis of an intermediate phase between sodalite and cancrinite', Catalyst Today, vol. 8, no. 4, pp. 415-426.

17. Barnes, M.C., Addai-Mensah, J., Gerson, A.R., 1999, 'The mechanism of the sodalite-to-cancrinite phase transformation in synthetic spent Bayer liquor', Microporous Mesoporous Materials, vol. 31, no. 3, pp. 287-302.

18. Kooli, F., Crespo, I., Barriga, C., Ulibarri, M.A., Rives, V., 1996, 'Precursor dependence of the nature and structure of nonstoichiometric magnesium aluminum vanadates', Journal of Materials Chemistry, vol. 6, no. 7, pp. 1199-1206.

19. Farmer, V.C., 1974, The Infrared spectra of minerals, Mineralogical Society, London.

20. Frost, R.L., Kloprogge, J.T., Russell, S.C., Szetu, J., 1999, 'Vibrational spectroscopy and dehydroxylation of aluminum (Oxo)hydroxides: gibbsite', Applied Spectroscopy, vol. 53, no 4, pp 423-434.

21. Marel, H.W. van der, Beutelspacher, H., 1976 Atlas of Infrared spectroscopy of clay minerals and their admixtures, Elsevier Scientific Pub. Co., New York.

22. Rochester, C.H., Topham, S.A., 1979, 'Infrared study of surface hydroxyl groups on hematite', Journal of Chemical Society, Faraday Transactions, vol. 75, pp. 1073-1088.

23. Gadsden, J.A., 1975, Infrared Spectra of Minerals and Related Inorganic Compounds, Butterworths, London.

24. Hunt, G.R., Ashley, R.P., 1979, 'Spectra of altered rocks in the visible and near infrared', Economic Geology and the Bulletin of the Society of Economic Geologists, vol. 74, no. 7, pp. 1613-1629.

25. Townsend, T.E., 1987, 'Discrimination of iron alteration minerals in visible and near-infrared reflectance data', Journal of Geophysical Research, vol. 92, no 2, pp. 1441-1454.

26. Marfunin, A., 1979, Physics of minerals and inorganic materials: an introduction, Springer-Verlag, New York.

27. Rossman, G.R., 1975, 'Spectroscopic and magnetic studies of ferric iron hydroxy sulfates. Intensification of colour in ferric iron clusters bridged by a single hydroxide ion', American Mineralogist, vol. 60, no. 7-8, pp. 698-704.

28. Rossman, G.R., 1976, 'Spectroscopic and magnetic studies of ferric iron hydroxy sulfates: the series $Fe(OH)SO_4.nH_2O$ and the jarosites', American Mineralogist, vol. 61, no. 5-6, pp. 398-404.

29. Tanabe, Y., Sugano, S., 1954, 'The absorption spectra of complex ions', Journal of the Physical Society of Japan, vol. 9, pp. 753-766.

30. Swayze, G.A., Clark, R.N., 1990, 'Infrared spectra and crystal chemistry of scapolites: Implications for Martian mineralogy', Journal of Geophysical Research, vol. 95, no. 9, pp. 14481-14495.

31. Reddy, B.J., Frost, R.L., 2007, 'Near infrared spectroscopy of aurichalcite $(Zn,Cu2+)5(CO3)2(OH)6$', Journal of Near Infrared Spectroscopy, vol. 15, no. 2, pp. 115-121.